



## Rational design of core-shell-structured $\text{CoP}_x\text{@FeOOH}$ for efficient seawater electrolysis

Libo Wu<sup>a,b</sup>, Luo Yu<sup>a</sup>, Brian McElhenny<sup>a</sup>, Xinxin Xing<sup>c</sup>, Dan Luo<sup>a</sup>, Fanghao Zhang<sup>a</sup>, Jiming Bao<sup>c</sup>, Shuo Chen<sup>a,\*</sup>, Zhifeng Ren<sup>a,\*</sup>

<sup>a</sup> Department of Physics and Texas Center for Superconductivity at the University of Houston (TcSUH), University of Houston, Houston, TX, 77204, USA

<sup>b</sup> Materials Science and Engineering Program, University of Houston, Houston, TX, 77204, USA

<sup>c</sup> Department of Electrical and Computer Engineering, University of Houston, Houston, TX, 77204, USA

### ARTICLE INFO

#### Keywords:

Core-shell structure  
Iron oxyhydroxide  
Cobalt phosphide  
Oxygen evolution reaction  
Seawater electrolysis

### ABSTRACT

Hydrogen generation by seawater electrolysis is a sustainable approach to renewable-energy conversion which requires efficient catalyst to address challenges such as competing chlorine evolution reaction, chloride corrosion, and catalyst poisoning. Here, core-shell-structured  $\text{CoP}_x\text{@FeOOH}$  is designed for selective OER in seawater. This catalyst has high conductivity, large surface area, improved turnover frequency, and optimal absorption energy to OER intermediates, which together lead to excellent catalytic activity. The enhanced chemical stability and corrosion resistance ensure its catalytic performance in seawater. Specifically, it requires overpotentials of 283 and 337 mV to attain current densities of 100 and 500  $\text{mA cm}^{-2}$ , respectively, in 1 M KOH seawater, with durability over 80 h of continuous testing without producing any hypochlorite. The  $\text{CoP}_x\text{||CoP}_x\text{@FeOOH}$  pair requires voltages of 1.710 and 1.867 V to attain current densities of 100 and 500  $\text{mA cm}^{-2}$  with a high Faradaic efficiency, showing its great promise for fuel-gas production from seawater.

### 1. Introduction

Using electrolysis to generate high-purity hydrogen ( $\text{H}_2$ ) fuel gas from natural seawater is a promising energy-conversion approach to decrease the excessive use of fossil fuels [1–4]. Compared with freshwater electrolysis, which has been widely investigated for decades, seawater electrolysis has several clear advantages, such as inexhaustible resource reserves, easy combination with ocean-related renewable-energy technologies, and accompanying production of safe drinking water, all of which make it more appealing and have attracted growing research interest [5–10]. To make seawater electrolysis energy-efficient and cost-effective, highly active non-noble-metal-based catalysts for boosting the oxygen evolution reaction (OER) on the anode and the hydrogen evolution reaction (HER) on the cathode are in significant demand [11–13]. Especially the ones that can sustain industrial-scale current density ( $> 500 \text{ mA cm}^{-2}$ ) are more favorable for future large-scale  $\text{H}_2$  production from seawater [8,14–16]. However, achieving a high current density normally requires a large overpotential, under which condition the chloride ions in natural seawater ( $\text{Cl}^-$ ,  $\sim 0.5 \text{ M}$ ) could compete with the anodic OER to form hypochlorite

( $\text{ClO}^-$ ), leading to lower seawater electrolysis efficiency [8,17–19]. The theoretical potential for hypochlorite formation in alkaline electrolyte is  $\sim 480 \text{ mV}$  higher than that for OER, which means that, without considering the extra overpotential needed to trigger the chlorine evolution reaction (ClER), the maximum overpotential applied on an OER catalyst should be lower than 480 mV in order to achieve 100 % seawater oxidation [6,10]. Besides enabling the competing ClER, chloride ions in natural seawater can corrode the catalyst, which is another critical challenge that needs to be addressed for long-term seawater electrolysis [8]. In addition, insoluble precipitates, either in the seawater itself (dust, colloids, and bacteria) or formed by the alkali metallic cations in the seawater reacting with the conductive reagent  $\text{OH}^-$  in the alkaline electrolyte [ $\text{Ca}(\text{OH})_2$  and  $\text{Mg}(\text{OH})_2$ ], will poison the catalyst and degrade its catalytic activity and durability [15,18].

Addressing the challenges mentioned above requires rational design of novel catalysts specifically for seawater electrolysis. For example, to meet the current density requirement for industrial hydrogen production while at the same time avoiding hypochlorite formation, the OER catalyst should have excellent catalytic activity to reach a high current density at an overpotential below 480 mV. Additionally, both the OER

\* Corresponding authors.

E-mail addresses: [schen34@uh.edu](mailto:schen34@uh.edu) (S. Chen), [zren@uh.edu](mailto:zren@uh.edu) (Z. Ren).

and HER catalysts should have high chloride-corrosion resistance and good structural stability to avoid electrode corrosion or collapse and thus maintain their catalytic activity in long-term seawater electrolysis. Finally, a hierarchical structured catalyst with a large surface area and abundant active sites is more favorable since insoluble precipitates in seawater might cover and deactivate some active sites. Among the catalysts explored for freshwater oxidation, iron oxyhydroxide (FeOOH), in which the oxyhydroxide species are considered to be the active sites for OER [20,21], is a promising one due to its merits, such as low cost, high intrinsic activity, and facile chemical composition tuning [22,23]. FeOOH-based catalysts such as amorphous FeOOH [22], (Ni,Fe)OOH [24], FeOOH(Se) [25], Ni<sub>3</sub>S<sub>2</sub>@MoS<sub>2</sub>/FeOOH [26], S-(Ni,Fe)OOH [15], and Ni-FeOOH@NiFe alloy [27] have been demonstrated to be efficient OER or bifunctional catalysts. However, pure-phase FeOOH still suffers from deficiencies like low conductivity, limited active sites, and excessively strong absorption energy to OER intermediates, all of which hinder their application in practical hydrogen production [25,28,29]. On the other hand, the self-supported cobalt-phosphide catalyst has features like tunable structure, excellent conductivity, and high thermal stability, making it a suitable HER catalyst for seawater electrolysis [17, 30–32].

Here, we employ heterogeneous cobalt phosphide (CoP<sub>x</sub>, CoP-CoP<sub>2</sub>) as the core to construct core-shell-structured CoP<sub>x</sub>@FeOOH as an efficient OER catalyst for seawater oxidation. Beyond their simple physical mixture, the combination of the highly conductive CoP<sub>x</sub> core and the OER-active FeOOH shell generates excellent synergistic effects such as high conductivity, large surface area, and improved turnover frequency. Insight analysis reveals that the negatively charged CoP<sub>x</sub> core can moderate the absorption energy between the oxyhydroxide active species and the OER intermediates to achieve very good intrinsic catalytic activity. Additionally, its micron-scale mesh structure and hydrophilic surface equip this CoP<sub>x</sub>@FeOOH catalyst with sufficient mechanical strength and high mass transfer efficiency at high current density. The catalyst's enhanced chloride corrosion resistance and chemical stability, which originate from the thermodynamically stable CoP<sub>x</sub> core, help it work well in seawater. Specifically, it requires overpotentials of only 235, 283, and 337 mV to attain current densities of 10, 100, and 500 mA cm<sup>-2</sup>, respectively, in 1 M KOH seawater electrolyte. It can sustain 80 h of continuous testing at current densities of 100 and 500 mA cm<sup>-2</sup> in alkaline seawater without forming any hypochlorite. When coupled with the HER-active CoP<sub>x</sub> core, the CoP<sub>x</sub>||CoP<sub>x</sub>@FeOOH pair requires low voltages of 1.710 and 1.867 V to attain current densities of 100 and 500 mA cm<sup>-2</sup>, respectively, with a high Faradaic efficiency and long-term catalytic durability. In general, this work demonstrates a novel strategy for the design and preparation of promising catalysts for efficient seawater electrolysis.

## 2. Experimental section

### 2.1. Synthesis of catalysts

#### 2.1.1. Synthesis of Co(OH)<sub>2</sub> nanowire mesh

Co(OH)<sub>2</sub> nanowire mesh was *in situ* grown on commercial nickel foam (NF, 35 mg cm<sup>-2</sup>) using a modified hydrothermal reaction based on previous reports [30,33]. Briefly, 2 mmol cobalt nitrate hexahydrate [Co(NO<sub>3</sub>)<sub>2</sub>·6H<sub>2</sub>O, Sigma Aldrich], 10 mmol urea [CO(NH<sub>2</sub>)<sub>2</sub>, Promega Corporation], and 5 mmol ammonium fluoride (NH<sub>4</sub>F, Alfa Aesar) were dissolved homogeneously in 60 mL deionized (DI) water. After stirring for 15 min, the mixed solution and a piece of cleaned NF (3 cm × 3.5 cm) were put into a 100 mL Teflon-lined stainless steel autoclave, which was then transferred to an oven maintained at 120 °C for 6 h. After cooling down to room temperature, the sample was removed from the autoclave and rinsed several times with DI water. The loading mass of the active material was measured to be 2.21 mg cm<sup>-2</sup>.

#### 2.1.2. Synthesis of CoP<sub>x</sub> nanowire mesh

To synthesize CoP<sub>x</sub> nanowire mesh, 500 mg sodium hypophosphite monohydrate (NaH<sub>2</sub>PO<sub>2</sub>·H<sub>2</sub>O, Alfa Aesar) was placed upstream in a tube as the phosphorous source. The as-prepared Co(OH)<sub>2</sub> precursor was placed at the center of the tube, followed by phosphidation at 400 °C for 2 h under flowing argon. The product was denoted CoP<sub>x</sub> and the loading mass was measured to be 2.28 mg cm<sup>-2</sup>.

#### 2.1.3. Synthesis of core-shell-structured CoP<sub>x</sub>@FeOOH

To construct the core-shell-structured CoP<sub>x</sub>@FeOOH, FeOOH was electrodeposited on CoP<sub>x</sub> in a three-electrode configuration, in which the CoP<sub>x</sub>, a platinum plate, and a saturated calomel electrode (SCE) were used as the working, counter, and reference electrodes, respectively. The electrodeposition electrolyte was prepared by dissolving 15 mmol iron sulfate heptahydrate (FeSO<sub>4</sub>·7H<sub>2</sub>O, Sigma Aldrich) in 50 mL DI water under a continuous argon flow to prevent the oxidation of Fe<sup>2+</sup>. The electrodeposition parameter was set as -1.0 V vs. SCE for 2 min to synthesize the optimal CoP<sub>x</sub>@FeOOH sample. The loading mass of active material (FeOOH shell) was measured to be 1.82 mg cm<sup>-2</sup>.

To confirm the optimal deposition time of 2 min, other CoP<sub>x</sub>@FeOOH-*y* (*y* = 1, 4, and 8 min) samples were prepared via the same procedure except for the different deposition time. Pristine FeOOH was electrodeposited directly on NF (donated FeOOH) using the same electrodeposition procedure, and its loading mass was measured to be 1.33 mg cm<sup>-2</sup>. CoP<sub>x</sub>@CoOOH (CoOOH) and CoP<sub>x</sub>@NiOOH (NiOOH) were synthesized using the same procedure except for replacing the iron sulfate heptahydrate with cobalt nitrate hexahydrate [Co(NO<sub>3</sub>)<sub>2</sub>·6H<sub>2</sub>O, Sigma Aldrich] and nickel nitrate hexahydrate [Ni(NO<sub>3</sub>)<sub>2</sub>·6H<sub>2</sub>O, Sigma Aldrich], respectively, in the electrodeposition step.

#### 2.1.4. Synthesis of IrO<sub>2</sub> and Pt/C catalysts on NF

To prepare the IrO<sub>2</sub> and Pt/C electrodes, 40 mg active material (either iridium oxide or platinum on carbon) was uniformly dispersed in a mixture solution containing 90 μL Nafion solution, 810 μL ethanol, and 600 μL DI water with the assistance of intense ultrasonication. A piece of cleaned NF was then soaked in the solution for 1 h to let the active material coat the surface, followed by drying in air.

## 2.2. Chemical and structural characterization

X-ray diffraction (XRD, PANalytical X'pert PRO, Cu Kα radiation) was employed to identify the crystal structure and chemical composition of these as-prepared samples. X-ray photoelectron spectroscopy (XPS, PHI Quantera) was conducted to identify the valence states of the elements. Raman tests were conducted on a Horiba iHR320 Raman spectrometer using a He-Ne laser (excitation wavelength: 532 nm). Morphology characterization and energy-dispersive spectroscopy (EDS) analysis were performed using scanning electron microscopy (SEM, LEO 1525) and transmission electron microscopy (TEM, JEOL 2010 F). The wettability of pure NF, CoP<sub>x</sub>, and CoP<sub>x</sub>@FeOOH was tested by depositing seawater droplets onto the surface of each catalyst. The Zeta potential values of CoP<sub>x</sub>, FeOOH, and CoP<sub>x</sub>@FeOOH were measured on a Malvern Zetasizer Nano ZS using droplets of each active material in DI water.

## 2.3. Electrochemical characterization

The catalytic performance of these catalysts was evaluated on a Gamry Reference 600 electrochemical station using a three-electrode configuration in which a Pt plate and a carbon rod were used as the counter electrodes for OER and HER testing, respectively; a Hg/HgO electrode was used as the reference electrode; and each catalyst (the size of each active part in the electrolyte is 0.5–0.8 cm<sup>2</sup>) was used as the working electrode. After at least 100 cyclic voltammetry (CV) cycles were performed, the stable polarization curve was recorded with *iR* compensation in three types of electrolyte (1 M KOH, 1 M KOH + 0.5 M

NaCl, and 1 M KOH seawater) at a scan rate of  $2 \text{ mV s}^{-1}$ . The recorded potential ( $E_{\text{Hg}/\text{HgO}}$ ) was calibrated to the reversible hydrogen electrode (RHE) using the equation:  $E_{\text{RHE}} = E_{\text{Hg}/\text{HgO}} + 0.098 + 0.0591 \times \text{pH}$ . Electrochemical impedance spectroscopy (EIS) was performed at the overpotential of 300 mV for OER from 100 kHz to 0.01 Hz in 1 M KOH. To measure the electrochemically active surface area (ECSA) of the catalyst, CV cycling was performed at potentials ranging from 0.925 to 1.025 V vs. RHE with different scan rates (20 to  $100 \text{ mV s}^{-1}$ ). By plotting the capacitive current at 0.975 V vs. RHE against the scan rates, the double-layer capacitance ( $C_{\text{dl}}$ ) was obtained as half of the corresponding slope value and then the ECSA was derived from the equation:  $\text{ECSA} = C_{\text{dl}}/C_s$ , in which  $C_s$  is the specific capacitance for a flat surface ( $40 \mu\text{F cm}^{-2}$ ). For the OER durability test, 2000 and 5000 CV scans were performed between 1.075 and 1.525 V vs. RHE at a scan rate of  $100 \text{ mV s}^{-1}$  and the corresponding polarization curves were recorded before and after the CV cycling. The chronopotentiometric measurements were recorded at the current densities of 100 and  $500 \text{ mA cm}^{-2}$  in 1 M KOH and 1 M KOH seawater, respectively. Overall seawater/freshwater electrolysis were carried out in a H-type electrolyzer cell with  $\text{CoP}_x@/\text{FeOOH}$  as the anodic electrode ( $0.5 \text{ cm}^2$ ),  $\text{CoP}_x$  as the cathodic electrode ( $0.5 \text{ cm}^2$ ), and an anion-exchange membrane (Fumasep, FAA-3-PK-130) as the separator. Natural seawater was collected from Galveston Bay, Texas, USA ( $29.364^\circ\text{N}$ ,  $94.810^\circ\text{W}$ ), from which Mg and Ca salts were first mostly removed by adding 0.68 g  $\text{Na}_2\text{CO}_3$  into 100 mL natural seawater before

application. Corrosion polarization curves were obtained on a SP-200 Biologic electrochemical station in untreated natural seawater using SCE as the reference electrode.

#### 2.4. Calculation of TOF

The plots of current density for OER can be converted into turnover frequency (TOF) plots using the equation:  $\text{TOF} = j \times A / (4 \times F \times n)$ , in which  $j$  is the current density ( $\text{A cm}^{-2}$ ),  $A$  is the active surface area of each electrode ( $\text{cm}^2$ ), 4 represents a four-electron transfer process,  $F$  is the Faraday constant ( $96485.3 \text{ C mol}^{-1}$ ), and  $n$  is the amount of active sites (mol), which can be roughly evaluated by the loading mass and the molecular weight of the active material [33,34].

#### 2.5. Calculation of faradaic efficiency

Faradaic efficiency (FE) testing was conducted using the drainage method at a constant current density of  $500 \text{ mA cm}^{-2}$  in 1 M KOH seawater. FE was calculated by the equation:  $\text{FE} = V / [V_m \times i \times t / (n \times F)] \times 100\%$ , in which  $V$  is the volume of the gas products (L),  $V_m$  is the standard molar volume at room temperature ( $24.4 \text{ L mol}^{-1}$ ),  $i$  is the current (A),  $t$  is the time (s),  $n$  is the number of electrons needed to form a molecule of gas products (4 for  $\text{O}_2$  and 2 for  $\text{H}_2$ ), and  $F$  is the Faraday constant.

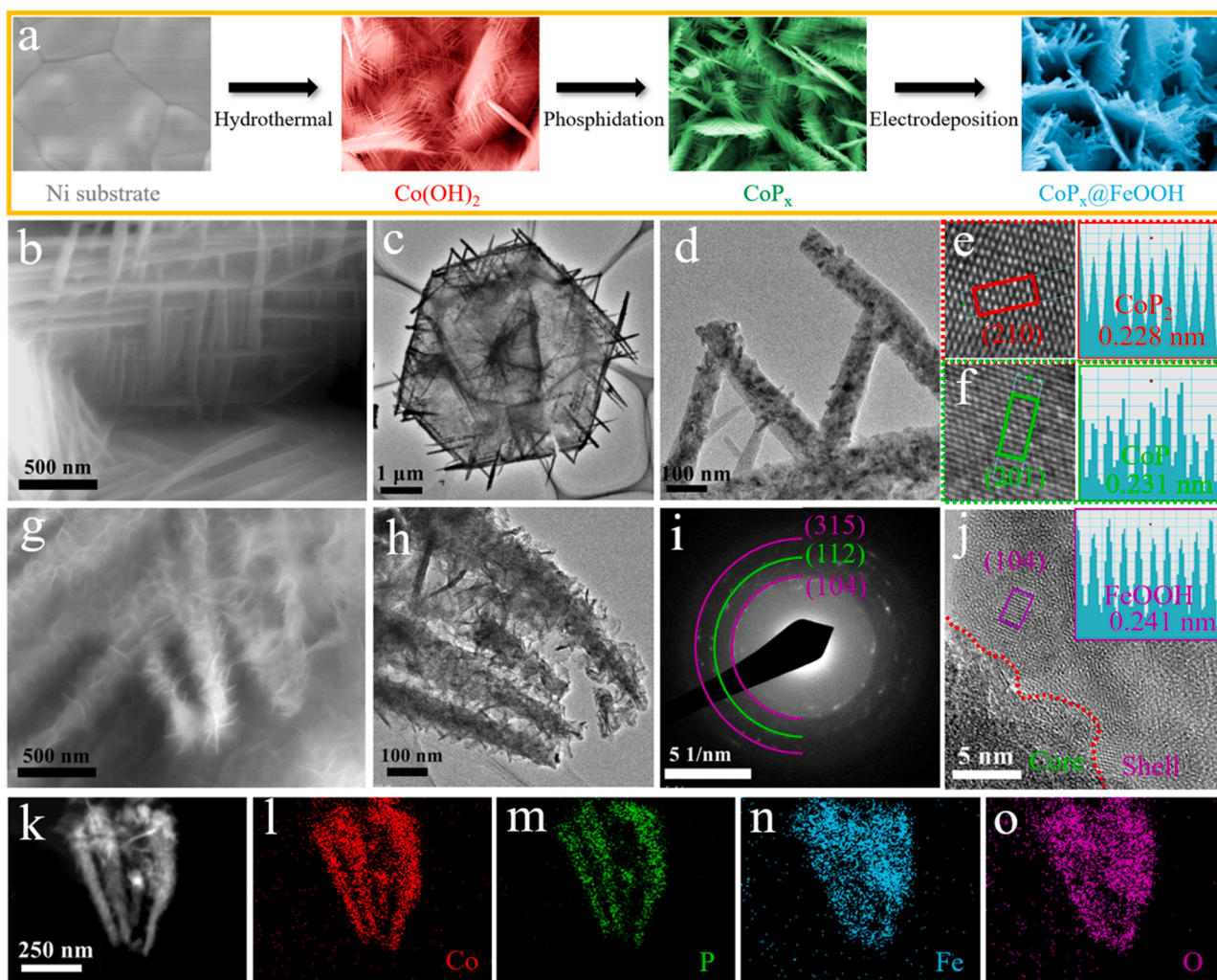


**Fig. 1.** (a) Schematic illustration of the synthesis of core-shell-structured  $\text{CoP}_x@/\text{FeOOH}$  via a three-step hydrothermal-phosphidation-electrodeposition procedure. (b) SEM, (c-d) TEM, and (e-f) HRTEM images of  $\text{CoP}_x$ . (g) SEM and (h) TEM images, (i) SAED pattern, and (j) HRTEM image of  $\text{CoP}_x@/\text{FeOOH}$ . (k) TEM image of a  $\text{CoP}_x@/\text{FeOOH}$  mesh and the corresponding EDX element mapping for (l) Co, (m) P, (n) Fe, and (o) O.

### 3. Results and discussion

#### 3.1. Characterizations of synthesized catalysts

As schematically illustrated in Fig. 1a, the core-shell-structured  $\text{CoP}_x@FeOOH$  catalyst was synthesized via a three-step hydrothermal-phosphidation-electrodeposition procedure (see the Experimental Section above). A self-supported  $\text{Co}(\text{OH})_2$  precursor was first *in situ* grown on conductive nickel foam (NF) using a modified hydrothermal reaction based on previous reports [30,33]. The scanning electron microscopy (SEM) images in Fig. S1 (Supplementary data) show numerous micron-scale  $\text{Co}(\text{OH})_2$  nanowire meshes, which are composed of cross-linked nanowires that are tens of nanometers in diameter, vertically stand on the entire surface of the NF substrate. This  $\text{Co}(\text{OH})_2$  precursor was then phosphated into  $\text{CoP}_x$  to enhance its conductivity, chloride corrosion resistance, and HER activity. The SEM images of  $\text{CoP}_x$  in Fig. 1b and S2a-c show that the nanowire mesh structure feature is well-preserved and the energy-dispersive spectroscopy (EDS) mapping images in Fig. S2d-e reveal that elemental Co and P are uniformly dispersed over the entire NF substrate, indicating a homogeneous and complete phosphidation. In the final step, an OER-active FeOOH shell was electrodeposited on the surface of the  $\text{CoP}_x$  to construct the core-shell-structured  $\text{CoP}_x@FeOOH$ . To determine the optimal electrodeposition time, four groups of  $\text{CoP}_x@FeOOH$ -y min (y = 1, 2, 4, and 8) samples were all prepared using the same routine except for different lengths of electrodeposition time. The FeOOH shell in these samples changes from a layer of film in  $\text{CoP}_x@FeOOH$ -1 min (Fig. S3a-d) to porous nanosheets in  $\text{CoP}_x@FeOOH$ -2 min (Fig. S4a-d), dense nanosheets in  $\text{CoP}_x@FeOOH$ -4 min (Fig. S3e-h), and nanospheres in  $\text{CoP}_x@FeOOH$ -8 min (Fig. S3i-l). Clearly, the morphology and structure of these  $\text{CoP}_x@FeOOH$ -y min samples can be tuned by adjusting the electrodeposition time. The open-structured  $\text{CoP}_x$  core with a FeOOH shell of suitable thickness will be beneficial for reducing the charge-transfer resistance and for exposing active material for catalytic reaction. Among all of these samples, the one prepared with 2-min electrodeposition time exhibits the best OER activity in 1 M KOH (Fig. S5), and it was selected as the representative sample for analysis and is specifically denoted  $\text{CoP}_x@FeOOH$  in the following discussion. Compared with the irregular film structure of pristine FeOOH (Fig. S6), the hierarchical structure of  $\text{CoP}_x@FeOOH$  can dramatically enlarge the surface area to expose more active sites during electrolysis, which is very important for achieving a high current density at a low overpotential. In addition, both  $\text{CoP}_x$  and  $\text{CoP}_x@FeOOH$  catalysts exhibit a hydrophilic feature for seawater as demonstrated in Fig. S7a-c and Fig. S7d-f, respectively, in sharp contrast with the pure Ni foam, which exhibits a hydrophobic feature as demonstrated in Fig. S7g-i. Some studies have illustrated that a hydrophilic surface is helpful for fast electrolyte diffusion and easy gas bubble release, which will be of great benefit in maintaining catalytic durability at high current density [9,14,35].

To characterize the structure of  $\text{CoP}_x$  and  $\text{CoP}_x@FeOOH$  in detail, transmission electron microscopy (TEM) analysis was performed. As shown in Fig. 1c-d and Fig. S8, the  $\text{CoP}_x$  nanowire meshes are consisted of linear smooth nanowires with diameters less than 100 nm and elemental Co and P are uniformly distributed throughout each nanowire. The interplanar spacings in the high-resolution TEM (HRTEM) images in Fig. 1e-f, which are precisely measured to be 0.228 and 0.231 nm, respectively, correspond to the respective (210) plane of  $\text{CoP}_2$  and the (201) plane of  $\text{CoP}$ , indicating that  $\text{CoP}_x$  is a mixture of heterogeneous cobalt phosphide ( $\text{CoP-CoP}_2$ ). As for the  $\text{CoP}_x@FeOOH$  catalyst, the SEM image in Fig. 1g and TEM image in Fig. 1h clearly shows that the  $\text{CoP}_x$  nanowire mesh core was completely covered by the porous FeOOH shell. The ring patterns from selected area electron diffraction (SAED) in Fig. 1i reveal the characteristic (112) facet of  $\text{CoP}$  and the (104) and (315) facets of FeOOH. Distinctive lattice fringes with interplanar spacings of 0.241 nm, which is assigned to the (104) plane of FeOOH, can be measured in the shell part in the HRTEM image shown in

Fig. 1j. The core-shell structure feature of the  $\text{CoP}_x@FeOOH$  catalyst can also be confirmed by the energy-dispersive X-ray spectrometry (EDX) mapping images in Fig. 1k-o, in which elemental Co and P (Fig. 1l-m, respectively) can only be observed in the core, while elemental Fe and O (Fig. 1n-o, respectively) can be observed over the entire selected area.

The exact chemical compositions of these as-prepared catalysts were detected by X-ray diffraction (XRD) testing. As respectively shown in Fig. S9a and S9b, the XRD curves of the  $\text{Co}(\text{OH})_2$  precursor and pristine FeOOH correspond to the standard PDF cards for cobalt hydroxide [ $\text{Co}(\text{OH})_2$ , JCPDS#50-0235] and iron oxyhydroxide (FeOOH, JCPDS#22-0353), respectively. The XRD pattern of  $\text{CoP}_x$  displayed in Fig. 2a shows that it is a mixture of two kinds of cobalt phosphide ( $\text{CoP}$ , JCPDS#29-0497 and  $\text{CoP}_2$ , JCPDS#22-0481), in good agreement with the HRTEM result. Besides the peaks for  $\text{CoP}$  and  $\text{CoP}_2$ , some extra peaks corresponding to iron oxyhydroxide (FeOOH, JCPDS#22-0353) can be found in the XRD pattern of  $\text{CoP}_x@FeOOH$  shown in Fig. 2a. To verify the compositions of FeOOH and  $\text{CoP}_x@FeOOH$  more accurately, Raman testing was then conducted and the corresponding results are shown in Fig. 2b. Compared with the sharp peaks in the Raman spectrum of pristine FeOOH, the peaks corresponding to iron oxyhydroxide in that of  $\text{CoP}_x@FeOOH$  are relatively lower in intensity due to the limited amount of iron oxyhydroxide on the shell [22,27,36,37]. X-ray photoelectron spectroscopy (XPS) was further performed in order to investigate the valence states of the elements in these catalysts. As shown in Fig. 2c, the high-resolution XPS spectra of Co 2p for  $\text{CoP}_x$  and  $\text{CoP}_x@FeOOH$  can be deconvoluted to a  $\text{Co}^{2+} 2p_{3/2}$  peak at 782.1 eV and a  $\text{Co}^{2+} 2p_{1/2}$  peak at 798.0 eV accompanied by a pair of satellite peaks [32,38,39]. A tiny metallic peak for Co at 777.8 eV can be observed in the XPS spectrum for  $\text{CoP}_x$ . As for the XPS spectra of P 2p (Fig. 2d), in addition to a huge oxidation peak for P-O at 134.5 eV, which is mainly caused by the oxidation of the metallic phosphide when being exposed to the air, the peaks for P  $2p_{3/2}$  at 128.3 eV and for P  $2p_{1/2}$  at 129.8 eV can only be identified in the  $\text{CoP}_x$  sample [18,32,40]. Due to the coverage by the FeOOH shell, the intensity of the Co and P peaks for  $\text{CoP}_x@FeOOH$  is relatively lower than that for  $\text{CoP}_x$ . The XPS spectra of Fe for  $\text{CoP}_x@FeOOH$  in Fig. 2e exhibit peaks for  $\text{Fe}^{3+} 2p_{3/2}$  at 711.5 eV and  $\text{Fe}^{3+} 2p_{1/2}$  at 724.3 eV along with a satellite peak at 718.6 eV [27]. Compared with those for pristine FeOOH, the Fe peaks for  $\text{CoP}_x@FeOOH$  are positively shifted to a higher oxidation state by  $\sim 0.3$  eV, which is considered more favorable for OER catalysis [34]. As shown in Fig. 2f, the peaks located at 529.3, 531.7, 532.8, and 533.6 eV in the XPS spectrum of O for  $\text{CoP}_x@FeOOH$  are assigned to oxygen-iron (O-Fe), hydroxide (O-H), chemisorbed water ( $\text{H}_2\text{O}$ ), and oxygen-phosphide (O-P), respectively [39,41].

#### 3.2. Catalytic performance of synthesized catalysts

##### 3.2.1. OER performance of $\text{CoP}_x@FeOOH$ in alkaline freshwater and seawater

These self-supported catalysts as well as the benchmark  $\text{IrO}_2$  catalyst were then directly used as working electrodes in a standard three-electrode configuration to evaluate their catalytic performance. For OER testing, all polarization curves were collected from high to low potential at a scan rate of  $2 \text{ mV s}^{-1}$  to avoid the oxidation-peak effect and to determine the overpotentials at small current densities precisely. As shown in Fig. 3a, the  $\text{CoP}_x@FeOOH$  catalyst displays catalytic activity for freshwater oxidation superior to that of  $\text{Co}(\text{OH})_2$ ,  $\text{CoP}_x$ , FeOOH, and  $\text{IrO}_2$ , requiring overpotentials of 222, 254, 292, and 303 mV to attain current densities of 10, 100, 500, and 800  $\text{mA cm}^{-2}$ , respectively, in 1 M KOH. Impressively, its Tafel slope value is calculated to be only  $37.6 \text{ mV dec}^{-1}$  (Fig. 3b), indicating a high transfer coefficient and rapid electrocatalytic kinetics. Such OER catalytic activity enables this  $\text{CoP}_x@FeOOH$  catalyst to outperform many self-supported oxyhydroxide, layered double hydroxide, and other catalysts reported to date (Table S1). Notably, to attain current densities of 10 and 100  $\text{mA cm}^{-2}$ , the second-best catalyst studied here, pristine FeOOH, requires

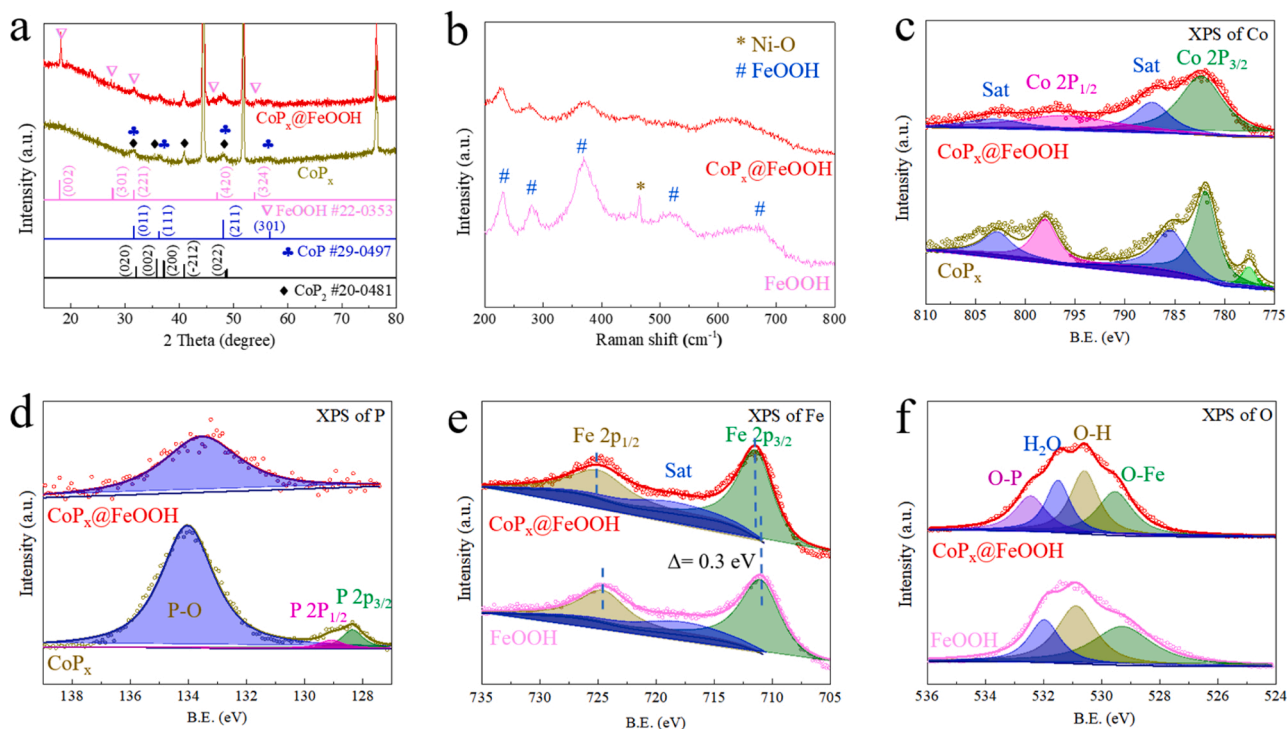


**Fig. 2.** (a) XRD patterns of CoP<sub>x</sub> and CoP<sub>x</sub>@FeOOH. (b) Raman spectra of pristine FeOOH and CoP<sub>x</sub>@FeOOH. High-resolution XPS spectra of (c) Co and (d) P in CoP<sub>x</sub> and CoP<sub>x</sub>@FeOOH and of (e) Fe and (f) O in FeOOH and CoP<sub>x</sub>@FeOOH.

overpotentials of 244 and 287 mV, respectively, lower than those for Co(OH)<sub>2</sub> (299 and 370 mV, respectively) and CoP<sub>x</sub> (297 and 346 mV, respectively), demonstrating higher intrinsic OER catalytic activity among oxyhydroxide-based catalysts in comparison with hydroxide- and phosphide-based ones. To reveal the origin of the excellent catalytic activity of CoP<sub>x</sub>@FeOOH, electrochemical impedance spectroscopy (EIS), electrochemically active surface area (ECSA), and turnover frequency (TOF) analyses were conducted. Based on the equivalent circuit in the EIS analysis (Fig. 3c) [42], the charge-transfer resistance ( $R_{ct}$ ) value of CoP<sub>x</sub> is calculated to be  $\sim 1.58 \Omega$ , much smaller than that of the Co(OH)<sub>2</sub> precursor ( $\sim 12.87 \Omega$ ), implying that phosphidation can dramatically enhance the charge transfer kinetics. Even coated by poorly conductive FeOOH, the  $R_{ct}$  value of CoP<sub>x</sub>@FeOOH only increases to  $\sim 2.51 \Omega$ , still lower than that of pristine FeOOH (5.13  $\Omega$ ), suggesting a remarkable enhancement in conductivity through the combination with the CoP<sub>x</sub> core. The ECSA of CoP<sub>x</sub>@FeOOH, which is proportional to its double-layer capacitance ( $C_{dl}$ ) shown in Fig. S10, is also significantly enlarged through the construction of its hierarchical core-shell structure. As shown in Fig. 3d, the ECSA of CoP<sub>x</sub>@FeOOH (242.5 cm<sup>2</sup><sub>ECSA</sub>) is around 2.5 times as large as that of pristine FeOOH (102.5 cm<sup>2</sup><sub>ECSA</sub>), proving that more active sites can be exposed for OER catalysis. Current density was then normalized for ECSA to reveal the intrinsic surface-area catalytic activity of these catalysts and the CoP<sub>x</sub>@FeOOH still exhibits the highest OER catalytic activity (Fig. S11). In addition, the TOF value for CoP<sub>x</sub>@FeOOH at the potential of 1.52 V vs. RHE is calculated to be 0.059 s<sup>-1</sup> (Fig. S12), which is around three times as high as that for pristine FeOOH (0.021 s<sup>-1</sup>), showing a much higher instantaneous efficiency for OER catalysis. According to the theoretical calculations in previous reports, pure-phase FeOOH has excessively strong adsorption ability toward the negatively charged OER intermediates (O\*, OH\*, and OOH\*), which hinders the dislocation of products [43–45]. It is reasonable that the negatively charged P atoms can repel these OER intermediates to reach an optimal absorption energy for the CoP<sub>x</sub>@FeOOH catalyst. This may explain why the core-shell-structured CoP<sub>x</sub>@FeOOH exhibits intrinsic catalytic activity that is much better than that of both pristine FeOOH and CoP<sub>x</sub>, as revealed by the ECSA and

TOF analyses.

Considering the excellent OER catalytic activity of the CoP<sub>x</sub>@FeOOH catalyst in alkaline freshwater, we then evaluated its performance for seawater oxidation in both alkaline saline (1 M KOH in 0.5 M NaCl water, simulated seawater) and alkaline natural seawater (1 M KOH seawater). As shown in Fig. S13a, the OER catalytic activity of the five studied catalysts is well maintained in 1 M KOH + 0.5 M NaCl despite a slight decline caused by the blocking of some active sites by the Cl<sup>-</sup>. When measured in 1 M KOH seawater, the polarization curves in Fig. 3e reveal that the CoP<sub>x</sub>@FeOOH catalyst requires overpotentials of 235, 283, 337, and 354 mV to attain current densities of 10, 100, 500, and 800 mA cm<sup>-2</sup>, respectively, much lower than the maximum potential ( $\sim 480$  mV) for avoiding the formation of hypochlorite. To assess the catalytic kinetics of these catalysts in each electrolyte, corresponding Tafel slope values are calculated (Fig. 3b and Fig. S13b-c) and summarized in Fig. S13d. Notably, all of these catalysts have increasing Tafel slope values in the same order of 1 M KOH, 1 M KOH + 0.5 M NaCl, and 1 M KOH seawater electrolytes, indicating that their catalytic kinetics and transfer coefficient values are slightly and severely lowered in saline and natural seawater, respectively. Additionally, both the catalytic activity and the Tafel slope values of these catalysts obtained in freshwater are very close to those obtained in simulated seawater but are much better than those obtained in natural seawater. Compared with simulated seawater (0.5 M NaCl in freshwater), natural seawater has a low conductivity and a more complicated composition, containing alkaline metal cations (Ca<sup>2+</sup>, Mg<sup>2+</sup>, Na<sup>+</sup>, K<sup>+</sup>), chloride ions (Cl<sup>-</sup>), sulfate ions (SO<sub>4</sub><sup>2-</sup>), insoluble precipitates (dust, colloids, and bacteria), etc. [7, 46, 47]. Thus, for study of seawater electrolysis, it is more reasonable to use the data obtained in natural seawater, although it is worse than that obtained in simplified simulated seawater. Compared with the FeOOH catalyst, which experiences a severe drop in its catalytic activity, the CoP<sub>x</sub>@FeOOH catalyst maintains its catalytic activity well in natural seawater, showing the great benefit from its high conductivity and hierarchical core-shell structure. To evaluate the catalytic activity of the CoP<sub>x</sub>@FeOOH catalyst under real application conditions [48], OER cyclic voltammetry (CV) curves without  $iR$  compensation were obtained

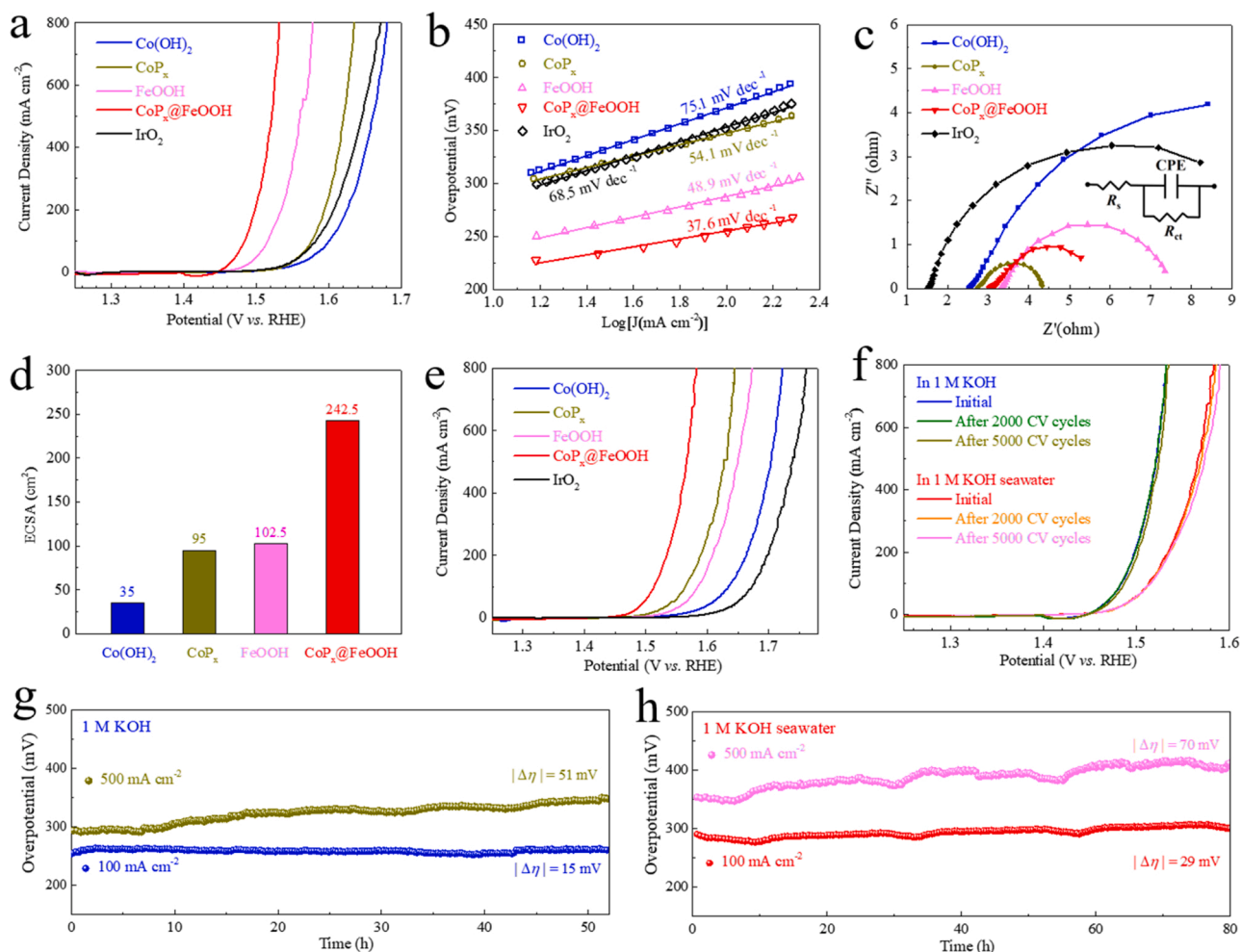


**Fig. 3.** (a) OER polarization curves of  $\text{Co}(\text{OH})_2$ ,  $\text{CoP}_x$ ,  $\text{FeOOH}$ ,  $\text{CoP}_x@FeOOH$ , and  $\text{IrO}_2$  catalysts in 1 M KOH electrolyte. (b) Tafel plots derived from the polarization curves in (a). (c) Nyquist plots and (d) ECSA values of these catalysts. (e) OER polarization curves of  $\text{CoP}_x@FeOOH$  before and after 2000 and 5000 CV scans in 1 M KOH and 1 M KOH seawater electrolytes. (f) OER polarization curves of  $\text{CoP}_x@FeOOH$  catalysts at constant current densities of 100 and 500  $\text{mA cm}^{-2}$  in (g) 1 M KOH and (h) 1 M KOH seawater electrolytes. Chronopotentiometric curves of  $\text{CoP}_x@FeOOH$  catalysts at constant current densities of 100 and 500  $\text{mA cm}^{-2}$  in (g) 1 M KOH and (h) 1 M KOH seawater electrolytes.

and are shown in Fig. S14.

The catalytic durability of the  $\text{CoP}_x@FeOOH$  catalyst were verified by both CV cycling and chronopotentiometric measurement in 1 M KOH and 1 M KOH seawater electrolytes. As shown in Fig. 3f, the CV cycling durability of this catalyst in 1 M KOH is confirmed by the nearly overlapping polarization curves obtained before and after 5000 CV cycles. A slight decline in the resultant polarization curves can be observed after cycling in 1 M KOH seawater due to the obstruction of active sites by  $\text{Cl}^-$  and the poisoning of the catalyst by insoluble precipitates. SEM images of the  $\text{CoP}_x@FeOOH$  catalyst after CV cycling in 1 M KOH seawater indicate that the core-shell structure on the micro scale (Fig. S15a-b) and the nanowire mesh structure on the macro scale (Fig. S15c-d) are both maintained, confirming good structural stability and high corrosion resistance. Corresponding high-resolution XPS spectra of the post-OER  $\text{CoP}_x@FeOOH$  catalyst (Fig. S16) show that elemental Fe on the shell is oxidized to a higher binding energy with lower intensity and a larger oxidation satellite peak while elemental Co and P in the core have higher intensities. The peaks refer to  $\text{FeOOH}$  phase disappeared in the XRD pattern of post-OER sample, indicating an amorphous phase was reconstructed on the surface [22,49]. This can be confirmed by the Raman spectra shown in Fig. S17, in which a pair of huge peaks refer to  $-\text{OOH}$  species appeared in the post-OER sample. Based on the XPS, XRD and Raman analysis, we can conclude that the OER active sites are  $\text{Fe}-\text{OOH}$  species in the reconstructed amorphous shell in the  $\text{CoP}_x@FeOOH$  catalyst. The chronopotentiometric measurement curves in

Fig. 3g-h show that the potential fluctuation of the  $\text{CoP}_x@FeOOH$  catalyst over 80 h continuous testing at a current density of 100  $\text{mA cm}^{-2}$  in 1 M KOH seawater is merely 29 mV, slight worse than its performance in 1 M KOH (15 mV over 50 h testing). When tested at the industrial-scale current density of 500  $\text{mA cm}^{-2}$ , this  $\text{CoP}_x@FeOOH$  catalyst can still work steadily despite some increase in the potential fluctuations (70 mV over 80 h testing and 51 mV over 50 h testing in 1 M KOH seawater and 1 M KOH electrolytes, respectively). These low potential fluctuations at such a high current density for such long testing durations place the  $\text{CoP}_x@FeOOH$  catalyst among the best self-supported catalysts for seawater electrolysis reported thus far (Table S2). Following the stability test, the possibility of hypochlorite product formation in 1 M KOH seawater electrolyte was determined using a colorimetric reagent. As shown in Fig. S18, there is no color change in the reagent, indicating there no hypochlorite was formed during OER stability testing.

### 3.2.2. HER performance of $\text{CoP}_x$ in alkaline seawater

It is widely accepted that phosphide-based catalysts normally have high HER catalytic activity because the P atoms can trap  $\text{H}^*$  intermediates and easily dissociate  $\text{H}_2$  molecules [30,50–52]. In particular, the  $\text{CoP}_x$  catalyst in this work, due to its heterogeneous phase composition ( $\text{CoP}-\text{CoP}_2$ ) with a higher ratio of P atoms compared to pure-phase  $\text{CoP}$ , has relatively more active sites (either defective phase interfaces or P atoms) for HER catalysis [32,38,51,53]. Additionally, the

nanowire mesh structure not only can expose each nanowire for contact and reaction with the electrolyte, but also provides sufficient mechanical strength when these nanowires cross one another to form a micron-scale mesh. When working as a cathodic electrode, the  $\text{CoP}_x$  catalyst exhibits much higher HER catalytic activity in 1 M KOH seawater than the other three self-supported catalysts, requiring low overpotentials of 117, 190, 248, and 269 mV to attain current densities of 10, 100, 500, and 800  $\text{mA cm}^{-2}$ , respectively, with an acceptable Tafel slope value of 71.1  $\text{mV dec}^{-1}$  (Fig. 4a and Fig. S19e-f). It exhibits even better HER catalytic activity in 1 M KOH (Fig. S19a-b) and 1 M KOH + 0.5 M NaCl (Fig. S19c-d). The catalyst's vertically standing nanowire mesh structure and its hydrophilic surface can promote electrolyte diffusion and  $\text{H}_2$  bubble release, leading to excellent catalytic durability and structural stability in 1 M KOH seawater electrolyte [14, 35], which is proved by the negligible decline in the resultant polarization curve after CV cycling (Fig. S20a), the stable chronopotentiometric measurement (Fig. 20b), and the well-maintained nanowire mesh structure observed after CV cycling (Fig. S21). Additionally, both the HER activity of the  $\text{CoP}_x/\text{NF}$  catalyst and the OER activity of the  $\text{CoP}_x@/\text{FeOOH}/\text{NF}$  catalyst are better than those of the  $\text{Ni-Co-P}/\text{NF}$  and  $\text{Ni-Co-P}@/\text{FeOOH}/\text{NF}$  catalysts, respectively (Fig. S22).

### 3.2.3. Overall seawater splitting performance of $\text{CoP}_x||\text{CoP}_x@/\text{FeOOH}$ pair

Inspired by these exciting results, we then coupled the OER-active  $\text{CoP}_x@/\text{FeOOH}$  as the anode electrode and the HER-active  $\text{CoP}_x$  as the cathode electrode for overall seawater electrolysis. As shown in Fig. S23a and Fig. 4b, this  $\text{CoP}_x||\text{CoP}_x@/\text{FeOOH}$  pair requires voltages of 1.549, 1.710, 1.867, and 1.922 V to attain current densities of 10, 100, 500, and 800  $\text{mA cm}^{-2}$ , respectively, in 1 M KOH seawater. When measured in the 1 M KOH electrolyte, which is widely used in alkaline freshwater electrolysis studies, this pair requires voltages of only 1.478, 1.688, 1.833, and 1.881 V to attain the same respective current densities. The Faradaic efficiency (FE) of this pair for overall seawater electrolysis was measured at a constant current density of 500  $\text{mA cm}^{-2}$  using the drainage method shown in Fig. S23b. The resultant data was collected and is displayed in Fig. 4c, which shows that the produced  $\text{O}_2$  and  $\text{H}_2$  gas amounts nearly match the theoretical values, indicating the high FE (> 98 %) of this pair. Additionally, its catalytic durability was evaluated through CV cycling and chronopotentiometric measurement. As shown in Fig. 4d, this  $\text{CoP}_x||\text{CoP}_x@/\text{FeOOH}$  pair has incredible cycling stability in 1 M KOH electrolyte, which is proved by the slight difference in the polarization curves before and after 5000 CV scans. Although there is some decline when cycled in 1 M KOH seawater electrolyte, this pair still maintains excellent overall seawater electrolysis activity,

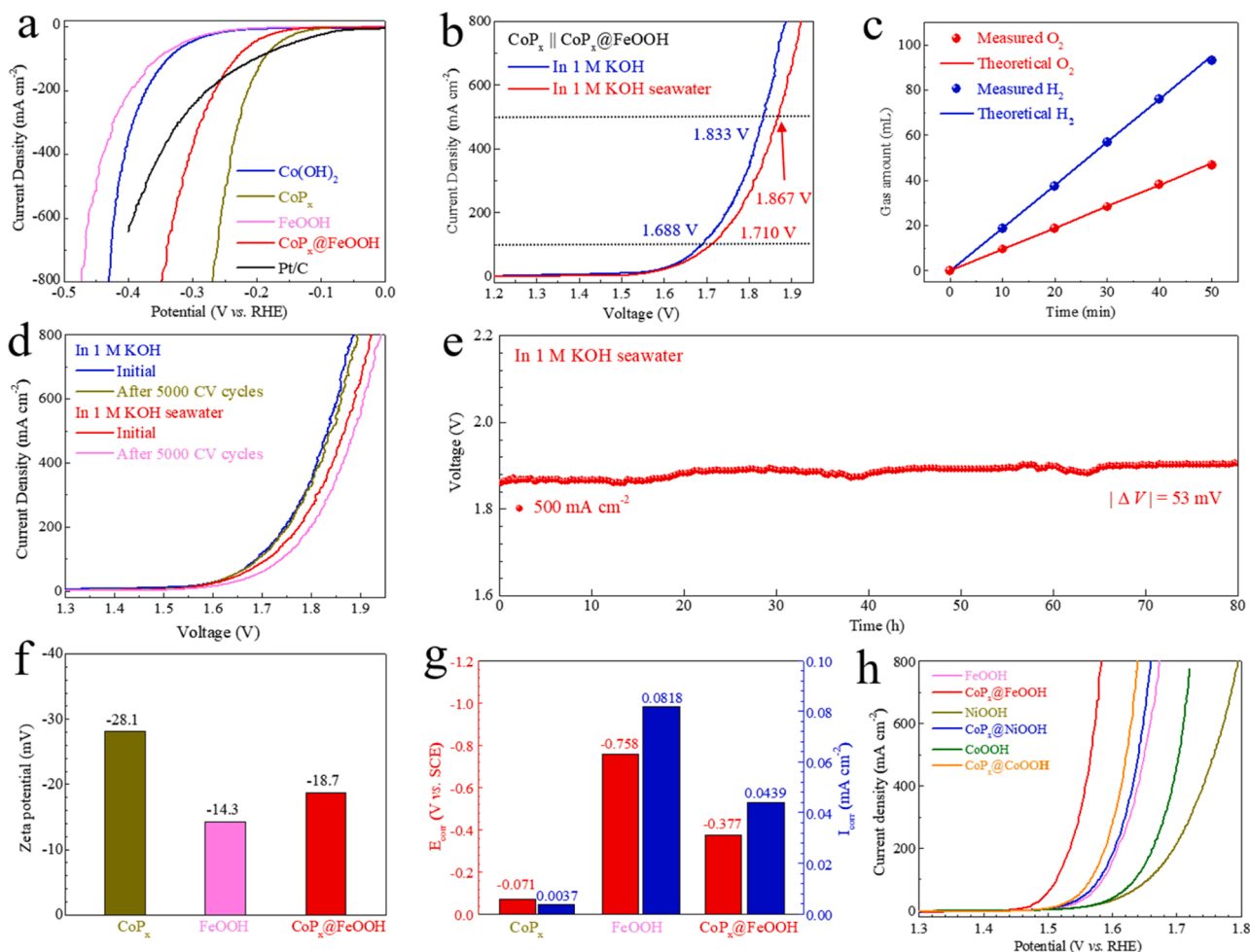


**Fig. 4.** (a) HER polarization curves of  $\text{Co}(\text{OH})_2$ ,  $\text{CoP}_x$ ,  $\text{FeOOH}$ ,  $\text{CoP}_x@/\text{FeOOH}$ , and  $\text{Pt}/\text{C}$  catalysts in 1 M KOH seawater electrolyte. (b) Overall freshwater/seawater electrolysis performance of the  $\text{CoP}_x||\text{CoP}_x@/\text{FeOOH}$  pair in 1 M KOH and 1 M KOH seawater electrolytes. (c) Measured (dots) and theoretical (solid lines) gaseous products from the  $\text{CoP}_x||\text{CoP}_x@/\text{FeOOH}$  pair at a current density of 500  $\text{mA cm}^{-2}$  in 1 M KOH seawater electrolyte. (d) Overall freshwater/seawater electrolysis performance of this pair before and after 5000 CV cycles in 1 M KOH and 1 M KOH seawater electrolytes. (e) Chronopotentiometric curve of the  $\text{CoP}_x||\text{CoP}_x@/\text{FeOOH}$  pair at a constant current density of 500  $\text{mA cm}^{-2}$  in 1 M KOH seawater electrolyte. (f) Zeta potentials of  $\text{CoP}_x$ ,  $\text{FeOOH}$ , and  $\text{CoP}_x@/\text{FeOOH}$  catalysts in natural seawater. (g) Corrosion potentials and corrosion current densities of  $\text{CoP}_x$ ,  $\text{FeOOH}$ , and  $\text{CoP}_x@/\text{FeOOH}$  catalysts in natural seawater. (h) OER polarization curves of  $\text{FeOOH}$ ,  $\text{CoP}_x@/\text{FeOOH}$ ,  $\text{CoOOH}$ ,  $\text{CoP}_x@/\text{CoOOH}$ ,  $\text{NiOOH}$ , and  $\text{CoP}_x@/\text{NiOOH}$  catalysts in 1 M KOH seawater electrolyte.

especially at large current densities. The catalytic durability of this pair is also proved by the results from a long-term chronopotentiometric measurement at an industrial-scale current density of  $500 \text{ mA cm}^{-2}$ , which show that it suffers a 53-mV potential fluctuation over 80 h continuous testing (Fig. 4e). Their high FE and excellent catalytic durability at such a high current density make  $\text{CoP}_x$  and  $\text{CoP}_x@FeOOH$  promising catalysts for realistic  $\text{H}_2$  production from natural seawater.

### 3.3. Chloride corrosion resistance analysis

Chloride corrosion is another severe challenge whose effect is difficult to determine during catalytic activity tests but will gradually take the center stage and limit the service life of a catalyst for seawater electrolysis. Here, the corrosion resistance performance of the  $\text{CoP}_x@FeOOH$  and  $\text{CoP}_x$  catalysts was first determined by a 25-day immersion test in natural seawater. As shown in Fig. S24 and Fig. S25, the structures of these two catalysts are well maintained after long-term immersion. For the  $\text{CoP}_x$  in particular, no obvious corrosion pits or structural collapse can be found, indicating its outstanding corrosion resistance and structural stability. In fact, the  $\text{CoP}_x$  catalyst can effectively repel the negatively charged  $\text{Cl}^-$  ions to reduce chloride corrosion due to its most negative Zeta potential (-28.1 mV) as shown in Fig. 4f. Compared with that of pristine  $FeOOH$  (-14.3 mV), the Zeta potential of  $\text{CoP}_x@FeOOH$  is lowered to -18.7 mV by coupling with the  $\text{CoP}_x$  core, enabling the enhanced chlorine-repelling ability of this core-shell-structured catalyst. To analyze the corrosion resistance of these catalysts in depth, corresponding corrosion polarization curves (Fig. S26) were collected in pure natural seawater without adding the conductive reagent KOH and the resultant data is summarized in Fig. 4g.  $\text{CoP}_x$  exhibits the highest corrosion potential (-0.071 V vs. SCE) and the lowest corrosion current density ( $0.0037 \text{ mA cm}^{-2}$ ) among all of the catalysts measured, indicating its highest chloride corrosion resistance ability. When incorporated into core-shell-structured  $\text{CoP}_x@FeOOH$ , the corresponding corrosion potential declines to -0.377 V vs. SCE and the corrosion current density increases to  $0.0439 \text{ mA cm}^{-2}$ , which are still much better than those of pristine  $FeOOH$  (-0.758 V vs. SCE and  $0.0818 \text{ mA cm}^{-2}$ , respectively). Both the Zeta potential and corrosion polarization curve analyses show that the  $\text{CoP}_x@FeOOH$  catalyst has remarkably enhanced chloride corrosion resistance compared with the pristine  $FeOOH$  catalyst. The alloying between the metallic Co and Fe cations and the P atoms can result in high thermodynamic stability and less metal dissolution, leading to enhancement in both chemical stability and corrosion resistance [18,51,52]. The  $\text{CoP}_x$  core in particular can act as a protection layer in the  $\text{CoP}_x@FeOOH$  catalyst to repel the chloride ions and reduce electrode corrosion. Thus, beyond a simple physical mixture, such a core-shell-structured  $\text{CoP}_x@FeOOH$  catalyst can effectively “hits two birds with one stone”, in which both the catalytic activity and chloride corrosion resistance are enhanced.

### 3.4. Discussion and expansion

With the limited supply of freshwater, seawater electrolysis is more appealing and has attracted tremendous research interest recently. However, due to critical challenges such as chlorine chemistry and catalyst poisoning, selective and stable catalysts are highly required for seawater electrolysis. Here, for the first time, we designed core-shell-structured  $\text{CoP}_x@FeOOH$  as an OER catalyst and a  $\text{CoP}_x$  nanowire mesh core as a HER catalyst for overall seawater electrolysis. Such a combination generates remarkable benefits to conquer the deficiencies of pure-phase  $FeOOH$  and thus can meet the requirement for selective seawater oxidation. First, besides enhancing the electron transport in the  $FeOOH$  shell, the micron-scale  $\text{CoP}_x$  core can provide sufficient mechanical strength and enlarge the surface area to rivet and expose more oxyhydroxide active sites for OER catalysis, which can address the low conductivity of, and insoluble precipitates in, natural seawater. Second, negatively charged P atoms in the  $\text{CoP}_x$  core can moderate the

absorption energy of the  $FeOOH$  active sites to OER intermediates, leading to high intrinsic catalytic activity, which can effectively avoid the CER and reach a high FE at industrial-scale current densities. Third, the employment of a binder-free NF substrate modified to exhibit a hydrophilic surface feature provides adequate space for electrolyte diffusion and accelerates bubble release, together ensuring the catalytic durability of  $\text{CoP}_x@FeOOH$  and  $\text{CoP}_x$  catalysts at high current densities. Fourth, when alloying with P atoms, both the chloride corrosion resistance and the structural stability of the  $\text{CoP}_x@FeOOH$  and  $\text{CoP}_x$  catalysts are enhanced due to their higher chlorine-repelling ability and less metal dissolution. The three-step hydrothermal-phosphidation-electrodeposition procedure described here can also be exploited to synthesize core-shell-structured  $\text{CoP}_x@CoOOH$  (Fig. S27) and  $\text{CoP}_x@NiOOH$  catalysts (Fig. S28) by simply changing the electrodeposition electrolyte to  $\text{Co}(\text{NO}_3)_2$  and  $\text{Ni}(\text{NO}_3)_2$  aqueous solutions, respectively. As shown in Fig. 4h, all of the core-shell-structured catalysts exhibit higher OER catalytic activity in alkaline seawater electrolyte than their counterparts directly electrodeposited on NF substrates, indicating that this may be an effective and universal method for synthesizing promising catalysts for seawater electrolysis.

## 4. Conclusion

We have successfully constructed core-shell-structured  $\text{CoP}_x@FeOOH$  as an efficient OER catalyst for seawater oxidation. Benefiting from the highly conductive and vertically standing  $\text{CoP}_x$  core as well as a hydrophilic surface, this hierarchical  $\text{CoP}_x@FeOOH$  catalyst exhibits enhanced conductivity, enriched active sites, sufficient mechanical strength, and accelerated bubble-release ability, all of which lead to superior OER catalytic activity at high current densities. In addition, the high chloride corrosion resistance and enhanced chemical stability help it work well in alkaline seawater electrolyte. When coupled with the HER-active  $\text{CoP}_x$  core, the  $\text{CoP}_x||\text{CoP}_x@FeOOH$  pair requires voltages of 1.710 and 1.867 V to attain current densities of 100 and  $500 \text{ mA cm}^{-2}$ , respectively, in 1 M KOH seawater electrolyte with high Faradaic efficiency and long-term stability. This work not only introduces and analyses catalysts for selective seawater electrolysis, but also provides opportunities in engineering the structure and corrosion chemistry to design more innovative catalysts for seawater electrolysis.

### CRediT authorship contribution statement

**Libo Wu:** Conceptualization, Methodology, Verification, Formal analysis, Investigation, Data curation, Writing - original draft. **Luo Yu:** Conceptualization, Methodology, Formal analysis. **Brian McElhenny:** Methodology, Formal analysis. **Xinxin Xing:** Data curation, Methodology, Formal analysis. **Dan Luo:** Data curation, Formal analysis. **Fan-gao Zhang:** Data curation, Formal analysis. **Jiming Bao:** Resources. **Shuo Chen:** Conceptualization, Methodology, Formal analysis, Writing - review & editing, Resources, Supervision. **Zhifeng Ren:** Conceptualization, Methodology, Formal analysis, Writing - review & editing, Resources, Supervision.

### Declaration of Competing Interest

The authors declare that they have no known competing financial interests or personal relationships that could have appeared to influence the work reported in this paper.

### Appendix A. Supplementary data

Supplementary material related to this article can be found, in the online version, at doi:<https://doi.org/10.1016/j.apcatb.2021.120256>.

## References

- [1] J.E. Bennett, *Int. J. Hydrogen Energy* 5 (1980) 401–408.
- [2] Z.W. Seh, J. Kibsgaard, C.F. Dickens, I. Chorkendorff, J.K. Nørskov, T.F. Jaramillo, *Science* 355 (2017) 6321.
- [3] I. Staffell, D. Scamman, A. Velazquez Abad, P. Balcombe, P.E. Dodds, P. Ekins, N. Shah, K.R. Ward, *Energy Environ. Sci.* 12 (2019) 463–491.
- [4] C. Wu, S. Xue, Z. Qin, M. Nazari, G. Yang, S. Yue, T. Tong, H. Ghasemi, F.C. R. Hernandez, S. Xue, D. Zhang, H. Wang, Z.M. Wang, S. Pu, J. Bao, *Appl. Catal. B Environ.* 282 (2021), 119557.
- [5] K. Fujimura, K. Izumiya, A. Kawashima, E. Akiyama, H. Habazaki, N. Kumagai, K. Hashimoto, *J. Appl. Electrochem.* 29 (1999) 769–775.
- [6] F. Dionigi, T. Reier, Z. Pawolek, M. Gliech, P. Strasser, *ChemSusChem* 9 (2016) 962–972.
- [7] S. Dresp, F. Dionigi, M. Klingenhof, P. Strasser, *ACS Energy Lett.* 4 (2019) 933–942.
- [8] Y. Kuang, M.J. Kenney, Y. Meng, W.-H. Hung, Y. Liu, J.E. Huang, R. Prasanna, P. Li, Y. Li, L. Wang, M.-C. Lin, M.D. McGehee, X. Sun, H. Dai, *Proc. Natl. Acad. Sci. U. S. A.* 116 (2019) 6624–6629.
- [9] L. Yu, Q. Zhu, S. Song, B. McElhenny, D. Wang, C. Wu, Z. Qin, J. Bao, Y. Yu, S. Chen, *Z. Ren, Nat. Commun.* 10 (2019) 5106.
- [10] W. Tong, M. Forster, F. Dionigi, S. Dresp, R. Sadeghi Erami, P. Strasser, A.J. Cowan, P. Farrás, *Nat. Energy.* 5 (2020) 367–377.
- [11] I.K. Mishra, H. Zhou, J. Sun, K. Dahal, Z. Ren, R. He, S. Chen, *Z. Ren, Mater. Today Phys.* 4 (2018) 1–6.
- [12] C. Huang, L. Yu, W. Zhang, Q. Xiao, J. Zhou, Y. Zhang, P. An, J. Zhang, Y. Yu, *Appl. Catal. B Environ.* 276 (2020), 119137.
- [13] H. Xu, H. Jia, B. Fei, Y. Ha, H. Li, Y. Guo, M. Liu, R. Wu, *Appl. Catal. B Environ.* 268 (2020), 118404.
- [14] Y. Luo, L. Tang, U. Khan, Q. Yu, H.M. Cheng, X. Zou, B. Liu, *Nat. Commun.* 10 (2019) 269.
- [15] L. Yu, L. Wu, B. McElhenny, S. Song, D. Luo, F. Zhang, Y. Yu, S. Chen, *Z. Ren, Energy Environ. Sci.* 13 (2020) 3439–3446.
- [16] S. Dresp, T. Ngo Thanh, M. Klingenhof, S. Brückner, P. Hauke, P. Strasser, *Energy Environ. Sci.* 13 (2020) 1725–1729.
- [17] J. Wang, W. Cui, Q. Liu, Z. Xing, A.M. Asiri, X. Sun, *Adv. Mater.* 28 (2016) 215–230.
- [18] L. Wu, L. Yu, F. Zhang, B. McElhenny, D. Luo, A. Karim, S. Chen, *Z. Ren, Adv. Funct. Mater.* (2020), 2006484.
- [19] L. Bigiani, D. Barreca, A. Gasparotto, T. Andreu, J. Verbeeck, C. Sada, E. Modin, O. I. Lebedev, J.R. Morante, C. Maccato, *Appl. Catal. B Environ.* 284 (2021), 119684.
- [20] H. Zhong, J. Wang, F. Meng, X. Zhang, *Angew. Chem., Int. Ed.* 55 (2016) 9937–9941.
- [21] A. Bergmann, T.E. Jones, E. Martinez Moreno, D. Teschner, P. Chernev, M. Gliech, T. Reier, H. Dau, P. Strasser, *Nat. Catal.* 1 (2018) 711–719.
- [22] W.D. Chemelewski, H.C. Lee, J.F. Lin, A.J. Bard, C.B. Mullins, *J. Am. Chem. Soc.* 136 (2014) 2843–2850.
- [23] S. Anantharaj, S. Kundu, S. Noda, *Nano Energy* 80 (2021), 105514.
- [24] H. Zhou, F. Yu, Q. Zhu, J. Sun, F. Qin, L. Yu, J. Bao, Y. Yu, S. Chen, *Z. Ren, Energy Environ. Sci.* 11 (2018) 2858–2864.
- [25] S. Niu, W.J. Jiang, Z. Wei, T. Tang, J. Ma, J.S. Hu, L.J. Wan, *J. Am. Chem. Soc.* 141 (2019) 7005–7013.
- [26] M. Zheng, K. Guo, W.-J. Jiang, T. Tang, X. Wang, P. Zhou, J. Du, Y. Zhao, C. Xu, J.-S. Hu, *Appl. Catal. B Environ.* 244 (2019) 1004–1012.
- [27] C. Liang, P. Zou, A. Nairan, Y. Zhang, J. Liu, K. Liu, S. Hu, F. Kang, H.J. Fan, C. Yang, *Energy Environ. Sci.* 13 (2020) 86–95.
- [28] W.T. Hong, M. Risch, K.A. Stoerzinger, A. Grimaud, J. Suntivich, Y. Shao-Horn, *Energy Environ. Sci.* 8 (2015) 1404–1427.
- [29] G. Chen, T. Wang, J. Zhang, P. Liu, H. Sun, X. Zhuang, M. Chen, X. Feng, *Adv. Mater.* 30 (2018), 1706279.
- [30] J. Tian, Q. Liu, A.M. Asiri, X. Sun, *J. Am. Chem. Soc.* 136 (2014) 7587–7590.
- [31] K. Xu, H. Cheng, H. Lv, J. Wang, L. Liu, S. Liu, X. Wu, W. Chu, C. Wu, Y. Xie, *Adv. Mater.* 30 (2018), 1703322.
- [32] H. Li, P. Wen, D.S. Itanze, M.W. Kim, S. Adhikari, C. Lu, L. Jiang, Y. Qiu, S. M. Geyer, *Adv. Mater.* 31 (2019), e1900813.
- [33] C. Tang, R. Zhang, W. Lu, L. He, X. Jiang, A.M. Asiri, X. Sun, *Adv. Mater.* 29 (2017), 1602441.
- [34] Y. Yang, L. Dang, M.J. Shearer, H. Sheng, W. Li, J. Chen, P. Xiao, Y. Zhang, R. J. Hamers, S. Jin, *Adv. Energy Mater.* 8 (2018), 1703189.
- [35] K. Dastafkan, Q. Meyer, X. Chen, C. Zhao, *Small* 16 (2020), e2002412.
- [36] D.L.A. de Faria, S. Venâncio Silva, M.T. de Oliveira, *J. Raman Spectrosc.* 28 (1997) 873–878.
- [37] M. Hanesch, *Geophys. J. Int.* 177 (2009) 941–948.
- [38] J. Cai, Y. Song, Y. Zang, S. Niu, Y. Wu, Y. Xie, X. Zheng, Y. Liu, Y. Lin, X. Liu, G. Wang, Y. Qian, *Sci. Adv.* 6 (2020) eaaw8113.
- [39] L. Yang, H. Li, Y. Yu, Y. Wu, L. Zhang, *Appl. Catal. B Environ.* 271 (2020), 118939.
- [40] W. Li, S. Zhang, Q. Fan, F. Zhang, S. Xu, *Nanoscale* 9 (2017) 5677–5685.
- [41] M. Fang, D. Han, W.B. Xu, Y. Shen, Y. Lu, P. Cao, S. Han, W. Xu, D. Zhu, W. Liu, J. C. Ho, *Adv. Energy Mater.* 10 (2020), 2001059.
- [42] S. Song, L. Yu, X. Xiao, Z. Qin, W. Zhang, D. Wang, J. Bao, H. Zhou, Q. Zhang, S. Chen, *Z. Ren, Mater. Today Phys.* 13 (2020), 100216.
- [43] K. Otte, W.W. Schmahl, R. Pentcheva, *J. Phys. Chem. C.* 117 (2013) 15571–15582.
- [44] B. Zhang, X. Zheng, O. Voznyy, R. Comin, M. Bajdich, M. García-Melchor, L. Han, J. Xu, M. Liu, L. Zheng, F.P. García de Arquer, C.T. Dinh, F. Fan, M. Yuan, E. Yassitepe, N. Chen, T. Regier, P. Liu, Y. Li, P. De Luna, A. Janmohamed, H.L. Xin, H. Yang, A. Vojvodic, E.H. Sargent, *Science* 352 (2016) 333–337.
- [45] G.-F. Chen, Y. Luo, L.-X. Ding, H. Wang, *ACS Catal.* 8 (2017) 526–530.
- [46] F.J. Millero, R. Feistel, D.G. Wright, T.J. McDougall, *Deep Sea Res. Part I Oceanogr. Res. Pap.* 55 (2008) 50–72.
- [47] L. Wu, L. Yu, Q. Zhu, B. McElhenny, F. Zhang, C. Wu, X. Xing, J. Bao, S. Chen, *Z. Ren, Nano Energy* (2021), 105838.
- [48] L. Yu, Z. Ren, *Mater. Today Phys.* 14 (2020), 100253.
- [49] X. Yu, Z.Y. Yu, X.L. Zhang, Y.R. Zheng, Y. Duan, Q. Gao, R. Wu, B. Sun, M.R. Gao, G. Wang, S.H. Yu, *J. Am. Chem. Soc.* 141 (2019) 7537–7543.
- [50] P. Xiao, M.A. Sk, L. Thia, X. Ge, R.J. Lim, J.-Y. Wang, K.H. Lim, X. Wang, *Energy Environ. Sci.* 7 (2014) 2624–2629.
- [51] Y. Shi, B. Zhang, *Chem. Soc. Rev.* 45 (2016) 1529–1541.
- [52] Y. Li, Z. Dong, L. Jiao, *Adv. Energy Mater.* 10 (2019), 1902104.
- [53] H. Xu, B. Fei, G. Cai, Y. Ha, J. Liu, H. Jia, J. Zhang, M. Liu, R. Wu, *Adv. Energy Mater.* 10 (2019), 1902714.